# Structural performance of axially- and laterally-loaded cantilevers with thermally-improved detailing

Kara D. Peterman [a,*], Justin Kordas [b], Mark D. Webster [c], Jim A. D'Aloisio [d], Jerome F. Hajjar [e]

[a] Department of Civil and Environmental Engineering, University of Massachusetts Amherst, 230 Marston Hall, 130 Natural Resources Way, Amherst, MA 01003, United States of America
[b] McNamara Salvia, Boston, MA, United States of America
[c] Simpson Gumpertz and Heger, Waltham, MA, United States of America
[d] Principal, Klepper Hahn and Hyatt, East Syracuse, NY, United States of America
[e] Department of Civil and Environmental Engineering, Northeastern University, Boston, MA, United States of America

## ARTICLE INFO

## ABSTRACT

Cladding details that span the building envelope are particularly susceptible to forming thermal bridges, where heat is transferred between interior and exterior, resulting in loss of energy. Steel buildings are particularly susceptible to forming thermal bridges due to the relatively high thermal conductivity of steel compared to that of other structural materials. To mitigate these thermal bridges, thermal breaks may be inserted in the cladding detail connection to the building interior, and have demonstrated promise in previous thermal modeling studies, with up to 65% reduction in thermal bridging. This paper summarizes recent work on the design, validation, and implementation of thermal break strategies that maintain structural integrity. Fiber-reinforced polymer (FRP) shims were used to provide thermal breaks in steel connections of cladding details. Partial replacement of steel structural members with FRP members was also explored. Shims were the focus of the work due to ease of installation, cross-section availability, and thermal performance. While several cladding details were examined in this research, this paper summarizes the cyclic performance of roof posts (under axial and cyclic lateral loads) and canopy beams (under cyclic lateral loads only), representing their anticipated performance during earthquakes and wind events. While roof posts and canopy beams exist in a range of applications in building construction, structural archetypes selected for this work represent lightly-loaded examples that are common in the field. The impact of adding FRP shims at the bolted base plate connection to the building interior is discussed. Recommendations for design and future research are also presented.

© 2021 Elsevier Ltd. All rights reserved.

## 1. Introduction

This research explores using thermal breaks to reduce energy loss when heating and cooling and to reduce condensation in steel building structures. Structural steel elements that pass through the building envelope can act as thermal bridges due to their ability to conduct heat, transferring interior heat or cooling to the exterior and thus increasing building energy consumption. Loss of energy through the building envelope can also cause condensation and negatively impact occupant comfort. The goal of this project is to explore and validate several concepts and develop associated design recommendations for mitigating the loss of energy via thermal bridging and other related issues in steel building structures by using a variety of possible solutions. While manufactured structural thermal break assemblies have gained traction worldwide, they can be cost-prohibitive for many projects. Proprietary products marketed as structural thermal breaks have struggled to gain

market share for this reason, in addition to a lack of interest in designing for building sustainability. By introducing thermal break strategies to various components throughout the detailing in a structure, we identify practical solutions geared for gaining acceptance and codification as needed for use within the steel construction industry. The scope of this work involves only snug-tight connections in structural steel roof posts to support dunnage and other systems on building roofs and cantilevered structural steel beams to support light canopies and other projecting elements. These types of structural components are often lightly loaded compared to the primary gravity and lateral or seismic force resisting systems of the structure. Experimental testing, structural analysis, and thermal analyses were conducted to explore a variety of solutions including different fiber-reinforced polymer (FRP) shims and manufactured structural thermal break assemblies (MSTBA). The focus of this paper is the structural performance of FRP shims installed as thermal breaks in structural steel elements which span the building envelope. These shims can be stacked in multiple plies to match insulation thickness, as shown in Fig. 1. Extensive thermal modeling efforts to validate the thermal performance of these shim details was explored in

* Corresponding author.
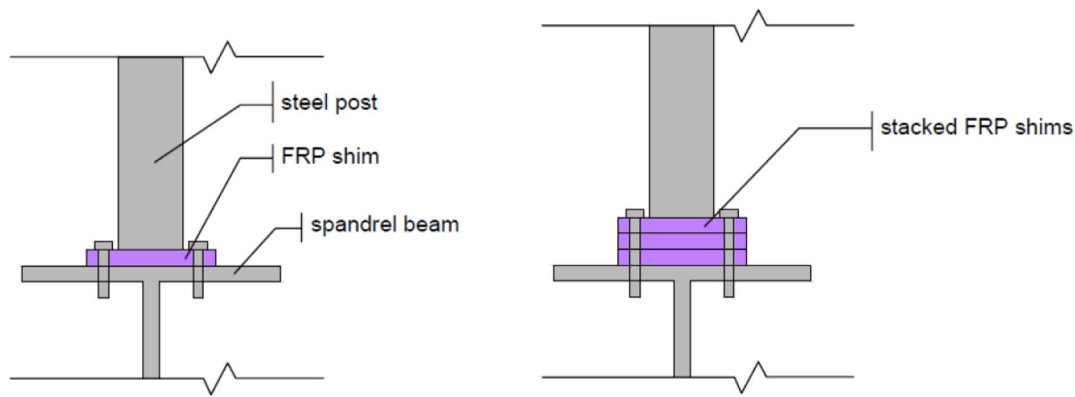  E-mail address: kdpeterman@umass.edu (K.D. Peterman).

**Fig. 1.** FRP shims stacked to varying thicknesses installed in the roof post-spandrel beam connection.

Peterman et al. [14]. The most effective thermal strategies were selected for the structural experiments summarized in this work.

White and Hamel [15] specifically examined the performance of cantilevered assemblies with thermally-improved detailing via a thermal hot box testing and modeling program followed by targeted structural experimental testing. The authors surveyed industry professionals across North America to determine their current practices in mitigating thermal bridging. Neoprene was identified as a popular and commonly-used thermal break in structural steel connections. As such, the authors conducted four experimental tests on steel cantilevers with varying thicknesses (ranging from 0 to 38.1 mm) of neoprene shims. The neoprene shims were identified to be detrimental to both structural and thermal performance. As neoprene shims increased in thickness, both strength and stiffness of the cantilevered assembly decreased significantly. As such, neoprene was excluded from the present study.

Morrison Hershfield [11] examined multiple thermal bridging solutions in envelope systems in steel and concrete buildings. This was a comprehensive study, including 40 common building envelope details in North America. Each detail was modeled via three-dimensional thermal modeling. The thermal modeling software was a research study variable, and results from three different software packages were provided, and calibrated against known thermal performance data. Most relevant to the present study, the Morrison Hershfield report included a steel cantilever spanning the building envelope (detail 12 in the report). For a given wall assembly, they found that a single beam penetration increases thermal transmittance by 9% and three beam penetrations increase transmittance by 25%.

The Corus Group [7] published findings on several thermal break strategies for use in steel structures. The Corus Group, a United Kingdom-based consulting firm, released a report in 2008 presenting the increase in transmittance due to thermal bridging in steel structures. The report examined the impact of localized insulation, slotted steel sections, stainless steel bolts, and proprietary manufactured thermal break assemblies. They observed modest improvements from localized insulation. Both slotted steel sections and stainless steel connections offered substantial improvement in thermal resistivity, but with compromises: reduced compressive and flexural capacity for the slotted steel, and increased risk of bi-metallic corrosion for the stainless bolts. The proprietary solution was observed to improve thermal resistance by 57%.

The work explored herein forms a portion of a larger effort, fully detailed in Peterman et al. [14], which includes thermal modeling, double-shear connection testing, base material testing, FRP creep testing, and computational modeling to validate and confirm experimental results. Roof posts and canopy beams both represent thermally discrete details in that they penetrate the building envelope at points, rather than along lines. Through the thermal modeling program, fiber reinforced polymer shims of all thicknesses improved thermal conductivity of the systems, though shims equal or greater in thickness to the insulation layer

were proven most thermally effective. Thus, shim thicknesses examined herein are aligned with recommended insulation thicknesses for two extremes: Climate Zones 1 and 7, as defined by ASHRAE 90.1 [3]. Full or partial replacement of the structural member with a fiber reinforced polymer member was also found to reduce heat flow at the building envelope. Thermal modeling demonstrated the efficacy of the proposed thermal break mitigation strategies. For discrete cladding details (i.e., roof posts and canopy beams), improvement in point thermal transmittance (defined in ASHRAE [4]) with an FRP shim installed is significant, with improvement between 60 and 70%, depending on climate zone and shim material. Another conclusion from the modeling effort was that thermal performance improved when the shim thickness matched or exceeded the insulation layer thickness.

Full or partial member replacement was explored in the experimental test program due to interest across the industry advisory panel. However, available pultruded fiber reinforced polymer shapes are available in limited sizes and thicknesses, especially when compared to steel shapes. Available sections preclude full member replacement as they are not thick enough to provide adequate capacity. In partial member replacement, connection fit-up between steel and composite members can be poor, resulting in additional flexibility in the system. While this could be mitigated with improved detailing, steel-to-FRP connections are not currently addressed in North American steel design specifications. Given these fabrication challenges, results are not reported herein, but can be found in [14].

## 2. Experimental setup and design

The structural archetypes and resulting test specimens are described below for both roof posts and canopy beams. Three "off-the-shelf" non-proprietary FRP plates were chosen: composites with glass fiber mats and vinylester, polyurethane, and phenolic resins. Two proprietary products were also included in the study, referred to as "proprietary 1" and "proprietary 2." Tested mechanical properties for the five FRP materials and steel base metals are summarized in Table 1, where E is the elastic modulus, $\sigma_{ys}$ the static yield stress, $\sigma_{yd}$ the dynamic yield stress, and $\sigma_u$ the ultimate stress. The roof post and canopy beam base metal was not tested, as the tensile coupons deformed during fabrication due to residual stresses in the HSS sections and could not be tested. As such, values from mill reports were used for the measured properties.

### 2.1. Experimental parameters and resultant test matrix

The test matrix for roof posts and canopy beams is presented in Table 2. Across specimen types, two configurations were considered: overdesigned specimens in which the fasteners, welds, and base plates are increased in size to prevent premature failure and to focus potential

**Table 1**
Mechanical properties for materials tested herein.

|  | E | $\sigma_{ys}$ | $\sigma_{yd}$ | $\sigma_u$ |
| --- | --- | --- | --- | --- |
|  | GPa | MPa | MPa | MPa |
| *Tensile properties* |  |  |  |  |
| 9.5 mm base plate | 223.2 | 283.2 | 320.4 | 454.3 |
| 12.7 mm base plate | 235.0 | 425.1 | 454.2 | 585.9 |
| A325 bolt | 215.0 | 868.6 | 903.9 | 1018 |
| ASTM A193 B8 class 2 bolt | 157.1 | 850.8 | 900.5 | 934.4 |
| ASTM A307 rod | 209.9 | – | 484.7 | 664.1 |
| *Compressive properties* |  |  |  |  |
| polyurethane | 4.27 | – | – | 411.7 |
| proprietary 1 | 3.10 | – | – | 272.2 |
| proprietary 2 | 3.45 | – | – | 269.9 |
| vinylester | 3.24 | – | – | 205.0 |
| phenolic | 0.69 | – | – | 114.1 |

range of potential responses in the base conditions, the base plates for efficiently-designed specimens were thinner than the common industry standard noted in the Design Guide, which is typically 19 mm (¾ in.).

Bolts were placed on the base plate at 152.4 mm (6 in.) on center, and were both efficiently designed with stainless steel ASTM A193 B8 Class 2 bolts [5], and overdesigned with 25.4 mm (1 in.) dia. ASTM A307 rods (in accordance with industry practices) [6]. Stainless bolts were specified to match A307 material properties, and represent one-to-one replacement of carbon steel fasteners with a thermally-improved alternative. Fasteners (used herein to collectively refer to bolts or rods) were installed by a single operator and were specified as snug-tight. Holes were specified as standard holes.

Roof posts were designed as HSS 76x76x4.8 (HSS 3x3x3/16 in.) while canopy beams were designed as HSS 102x102x12.7 (HSS 4x4x1/2 in.) (all HSS were specified as ASTM A500, Grade B (317 MPa

**Table 2**
Roof post and canopy beam test matrices.

| Test name | Specimen type | MITIGATION STRATEGY | | | SPECIMEN INFORMATION | | | | | Loading |
| --- | --- | --- | --- | --- | --- | --- | --- | --- | --- | --- |
|  |  | Type | Material | Thick | End Plate | Fastener Dia. | Fastener Spacing | Fastener Spec | | |
|  |  | – | – | mm | mm | mm | mm | – | | – |
| R1 | designed | – | – | – | 229x229x9.5 | 12.7 | 152.4 | B8 Class 2 | | Monotonic |
| R2 | designed | Shim | vinylester | 76.2 | 229x229x12.7 | 12.7 | 152.4 | B8 Class 2 | | Monotonic |
| R4 | designed | – | – | – | 229x229x9.5 | 12.7 | 152.4 | B8 Class 2 | | Cyclic |
| R5 | designed | Shim | vinylester | 76.2 | 229x229x12.7 | 12.7 | 152.4 | B8 Class 2 | | Cyclic |
| R7 | over-designed | – | – | – | 229x229x12.7 | 19.1 | 152.4 | A307 | | Cyclic |
| R8 | over-designed | Shim | vinylester | 76.2 | 229x229x12.7 | 19.1 | 152.4 | A307 | | Cyclic |
| R9 | over-designed | Shim | phenolic | 76.2 | 229x229x12.7 | 19.1 | 152.4 | A307 | | Cyclic |
| R10 | over-designed | Shim | polyurethane | 76.2 | 229x229x12.7 | 19.1 | 152.4 | A307 | | Cyclic |
| R11 | over-designed | Shim | proprietary 1 | 76.2 | 229x229x12.7 | 19.1 | 152.4 | A307 | | Cyclic |
| R12 | over-designed | Shim | proprietary 2 | 76.2 | 229x229x12.7 | 19.1 | 152.4 | A307 | | Cyclic |
| R13 | over-designed | Shim | vinylester | 25.4 | 229x229x12.7 | 19.1 | 152.4 | A307 | | Cyclic |
| R14 | over-designed | Shim | vinylester | 152.4 | 229x229x12.7 | 19.1 | 152.4 | A307 | | Cyclic |
| Test Name | Specimen Type | Type | Material | Thick | End Plate | Fastener Dia. | Fastener Spacing | Fastener Spec | | Loading |
|  |  | – | – | mm | mm | mm | mm | – | | – |
| C1 | designed | – | – | – | 229x229x9.5 | 19.1 | 152.4 | B8 Class 2 | | Monotonic |
| C2 | designed | Shim | vinylester | 76.2 | 229x229x9.5 | 19.1 | 152.4 | B8 Class 2 | | Monotonic |
| C4 | designed | – | – | – | 229x229x9.5 | 19.1 | 152.4 | B8 Class 2 | | Cyclic |
| C5 | designed | Shim | vinylester | 76.2 | 229x229x9.5 | 19.1 | 152.4 | B8 Class 2 | | Cyclic |
| C7 | over-designed | – | – | – | 229x229x12.7 | 25.4 | 152.4 | A307 | | Cyclic |
| C8 | over-designed | Shim | vinylester | 76.2 | 229x229x12.7 | 25.4 | 152.4 | A307 | | Cyclic |
| C9 | over-designed | Shim | phenolic | 76.2 | 229x229x12.7 | 25.4 | 152.4 | A307 | | Cyclic |
| C10 | over-designed | Shim | polyurethane | 76.2 | 229x229x12.7 | 25.4 | 152.4 | A307 | | Cyclic |
| C11 | over-designed | Shim | proprietary 1 | 76.2 | 229x229x12.7 | 25.4 | 152.4 | A307 | | Cyclic |
| C12 | over-designed | Shim | proprietary 2 | 76.2 | 229x229x12.7 | 25.4 | 152.4 | A307 | | Cyclic |
| C13 | over-designed | Shim | vinylester | 25.4 | 229x229x12.7 | 25.4 | 152.4 | A307 | | Cyclic |
| C15 | over-designed | Shim | vinylester | 152.4 | 229x229x12.7 | 25.4 | 152.4 | A307 | | Cyclic |

failure in the shims and the member; and, efficiently-designed specimens in which connections and base plates were designed to factored loads. Loads were based on an archetypal three-story steel building with composite floors (detailed in [14]). Roof posts were designed for typical dunnage loads, and canopy beams for self-weight and cladding. Shim thickness varied between 25.4, 76.2, and 152.4 mm (1, 3, and 6 in.) to align with potential insulation layer thicknesses.

Fig. 2 illustrates key experimental dimensions. Roof posts were designed to be 76.2 cm (2.5 ft) in height while canopy beams were designed to be 167.6 cm (5.5 ft) in length, both representing common construction configurations for their respective cladding details. Base plates were square to maintain symmetry in the experimental testing. Each plate was designed using the recommendations in the AISC Base Plate Design Guide [8]. It should be noted, however, that to explore a

or 46 ksi)). Posts and beams were of constant cross-section throughout the configurations tested. Welds between the post or beam and their respective base plate typically had the potential to be the critical limit state in these details, and as such, were detailed as complete joint penetration (CJP) welds to ensure they did not impact response in the design regime.

### 2.2. Test rig and protocol

The roof post/canopy beam test rig is comprised of two actuators, one horizontal (lateral) and one vertical, a load transfer block, the base (connecting specimen to the strong floor), and the reaction frame. These components are illustrated in Fig. 3.
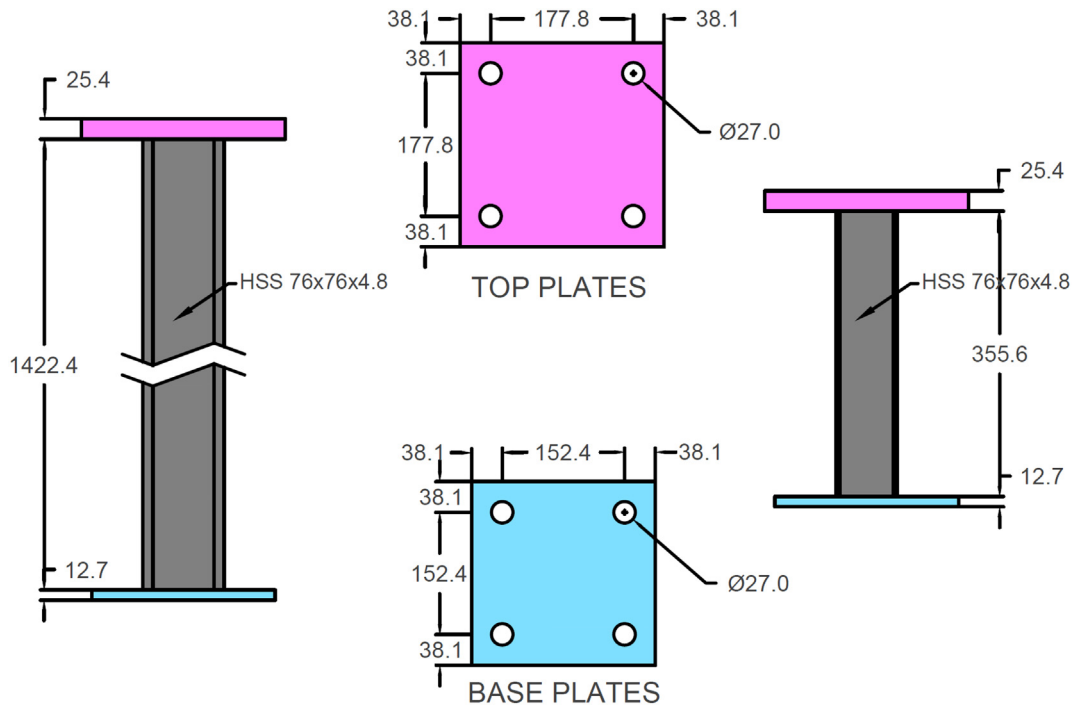
**Fig. 2.** Roof post (right) and canopy beam (left) specimen schematics. Dimensions in mm.

Roof posts are loaded with a 44.5 kN (10 kip) axial load in load control to replicate the weight of typical dunnage on the post. After the axial load is applied via the vertical actuator (in load control), the horizontal actuator loads the specimen in displacement control. Canopy beams are intended to be pure cantilevers with zero axial force. To achieve this condition, the vertical actuator counteracts the weight of the load transfer block and half of the horizontal actuator in load control so that the total axial force on the specimen is approximately zero. In both the

roof post and canopy beam test setups, the load transfer block is allowed to rotate to simulate a cantilever boundary condition, and is only restrained in the out-of-plane dimension.

Load is applied to the top of the specimen (connected to a 25.4 mm (1 in.) end plate using a CJP weld) via the load transfer block, which connects the two actuators to the top of the specimen using 25.4 mm (1 in.) dia. Bolts. The load block was designed to be rigid; this assumption was validated via isolated experimental testing by applying a large axial load
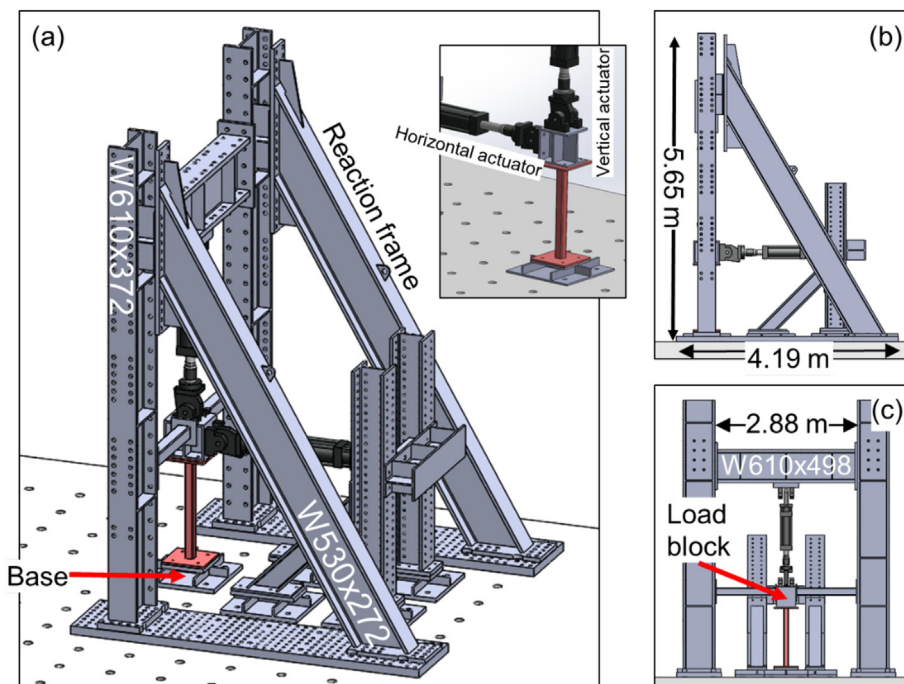


**Fig. 3.** Specimen positioned in the test rig at the Northeastern University STReSS Lab (a) isometric view of rig and specimen, inset demonstrates load application to specimen (b) side view (c) front view.

to the load block and confirming that there was negligible deformation. The horizontal actuator can move vertically up or down as needed, as can the vertical actuator. This feature allowed for specimens to vary in height according to shim thickness. This is illustrated in Fig. 4. To enable direct comparison across the specimens, the height of the steel beam-column was maintained for shimmed specimens. While Fig. 4 details this for roof posts, the same decisions were made for canopy beams, except the beam height is 1269.6 mm and 1422.4 mm for shimmed and unshimmed specimens, respectively. As discussed later in this section, the load protocol was modified for each specimen height to ensure each specimen was tested to comparable drifts.

Monotonic tests were displacement-controlled for the horizontal actuator, at a rate of 0.18% drift per minute while the vertical actuator remained in load control. Cyclic tests were displacement-controlled for the horizontal actuator, loading at a rate of 2.1% drift per minute, while the vertical actuator remained in load-control. Load rates were taken from the work of [9], in which steel posts with base plates were tested monotonically and cyclically. The cyclic protocol was adapted from Section K2.4b of AISC 341 [1,2] (reproduced here in Table 3), and was scaled to the total height of each specimen (which varied due to differing shim thicknesses – specimen heights used for this calculation are illustrated in Fig. 4) such that the load rate and drift targets were consistent across testing. Fig. 5 presents this protocol for the roof posts, depicting the scaling of the protocol for three different configurations. The actuator stroke is calculated by multiplying the specimen height (inclusive of shims) by the tangent of the story drift angle θ, presented in Table 3.

### 2.3. Instrumentation plan

To capture lateral movement of the base plate, linear variable differential transducers (LVDTs) were installed on the West face of the base plate (cardinal directions and specimen orientation are shown in Fig. 6 below). They were mounted to strong magnetic frames installed on the base of the rig. A set of five (quintuplet) LVDTs on the south and east sides of the base plate were oriented vertically to record the buckling of the base plate along its face on these two sides of the member. These quintuplet sensors recorded base plate deformed shapes up until approximately 2% drift, when they became misaligned with the base plate due to large deformations and were removed from the specimen. These quintuplets were also mounted via strong magnetic mounting frames affixed to the base of the rig.

Using small LVDTs installed along the longitudinal (vertical) dimension of the post/beam, it is possible to calculate the curvature of the post. Two LVDTs were installed along the east and west faces of the HSS specimens. The LVDTs overlapped such that their gage lengths were staggered. They were mounted to the HSS itself via aluminum brackets

**Table 3**
Cyclic load protocol as defined by AISC 341 [1,2]. For load steps beyond those presented herein, cycles increase in increments of 0.01θ until failure of the specimen.

| Load step # | Story drift angle θ | # of cycles, n |
|---|---|---|
| 1 | 0.00375 | 6 |
| 2 | 0.005 | 6 |
| 3 | 0.0075 | 6 |
| 4 | 0.01 | 4 |
| 5 | 0.015 | 2 |
| 6 | 0.02 | 2 |
| 7 | 0.03 | 2 |
| 8+ | 0.04 + (0.01θ) | 2 |

that were adhered to the specimen. While the original intent of installing these sensors was to capture post curvature, the most significant deformation was ultimately limited to the base plate, fasteners, and heat-affected zone of the weld. Thus, the roof post and canopy beam HSS did not experience measurable curvature along a significant portion of their length.

Strain gauges were also installed on each specimen. A strain gage was installed on the south and east faces of the base plate, 25.4 mm (1 in.) away from the weld to the post. Strain gauges staggered at 50.8 mm (2 in.) and 101.6 mm (4 in.) up from the base plate were installed on the post/beam on both the west and east sides of the specimen. These gauges were intended to provide curvature readings at ranges smaller than what the post/beam LVDTs can reliably record. Fig. 6 provides an illustration of the instrumentation plan. Fig. 7 depicts the sensors as-installed on a test specimen.

Washer load cells were fabricated and installed on each of the base plate fasteners. Load cells were 6.35 mm thick and had diameters matching those of the nuts installed on the fasteners. Each had four strain gauges installed on the washer thickness to record fastener tension. Strain gauge locations aligned with the cardinal directions in Fig. 6. Load cells were calibrated in a universal testing machine.

### 3. Results and discussion

Roof post results are presented in Table 4 for nominal test-to-predicted ratios, and Table 5 for measured test-to-predicted ratios using measured properties (Table 1). Maximum experimental loads ($P_u$) and moments ($M_u$) are included, as well as base plate yielding ($P_n$), post bending ($M_n$), shim compression ($P_{BA}$), fastener tension ($T_{bn}$), fastener shear ($T_n$), and fastener bending limit states ($M_{bn}$). Generally, n subscripts denote predicted values while u subscripts denote experimental values. To determine the experimental maximum moment, a reduction factor is applied to the height of the specimen (specimen height, h, is measured from the top of base plate to base of load
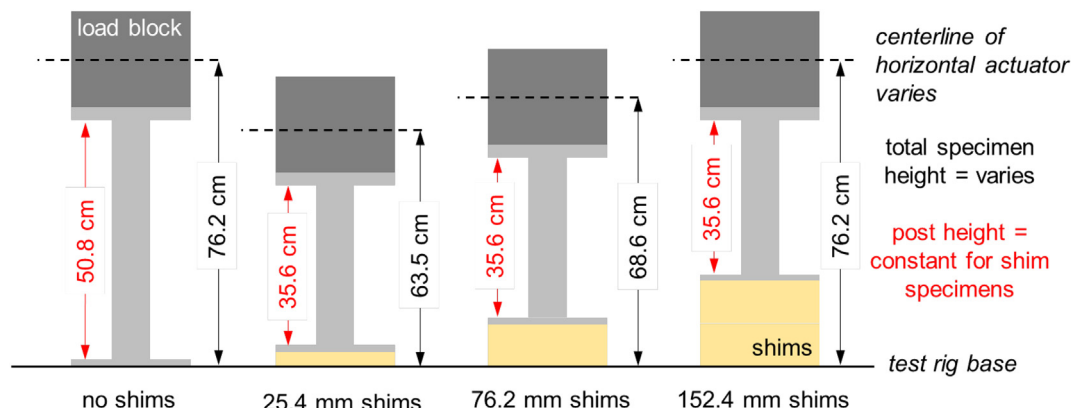


**Fig. 4.** Test configuration in which the post height is maintained for specimens with shims, and the horizontal actuator moved to accommodate the change in specimen height.
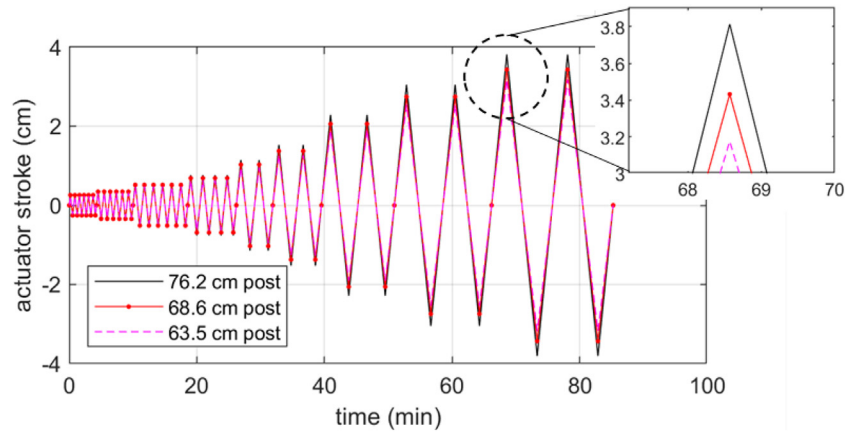
**Fig. 5.** Cyclic loading protocol scaled for various roof posts height such that load rate (2.1% drift/min) is constant throughout testing.
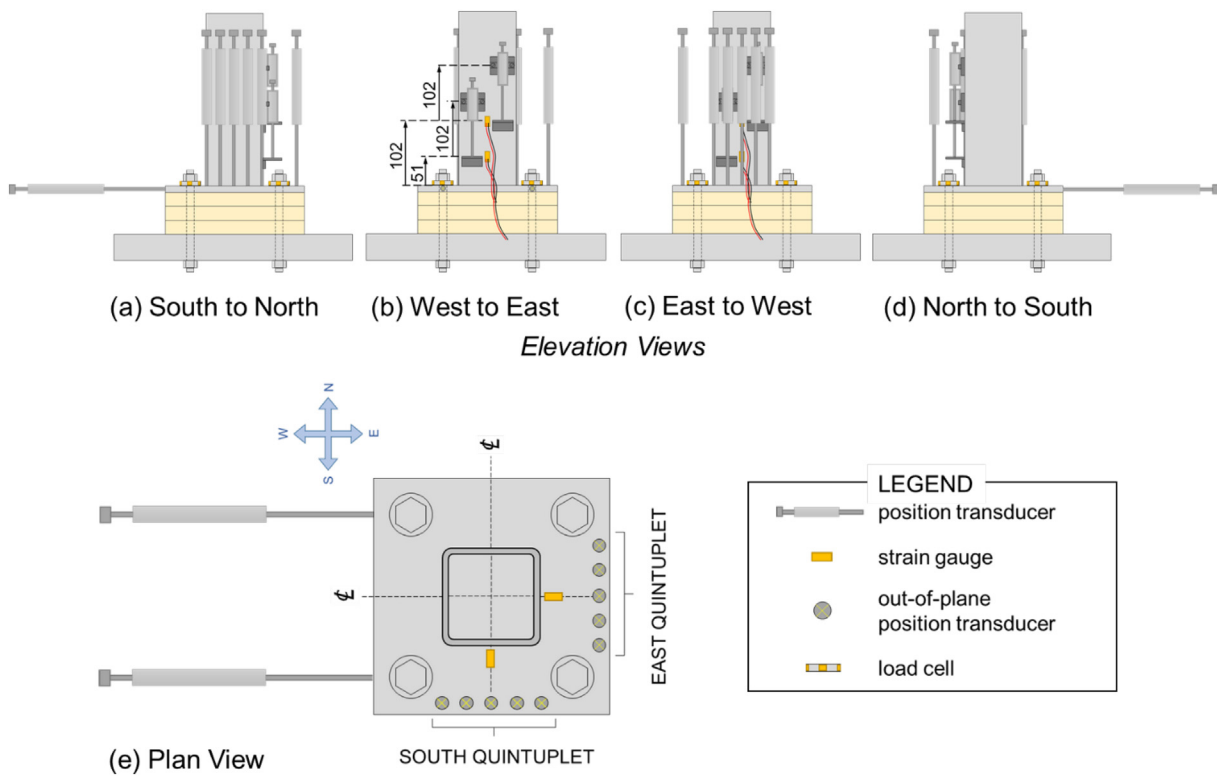


**Fig. 6.** Sensor configuration for roof post and canopy beam specimens, with elevation views((a) through (d)) in each direction and (e) plan view. Dimensions in mm.
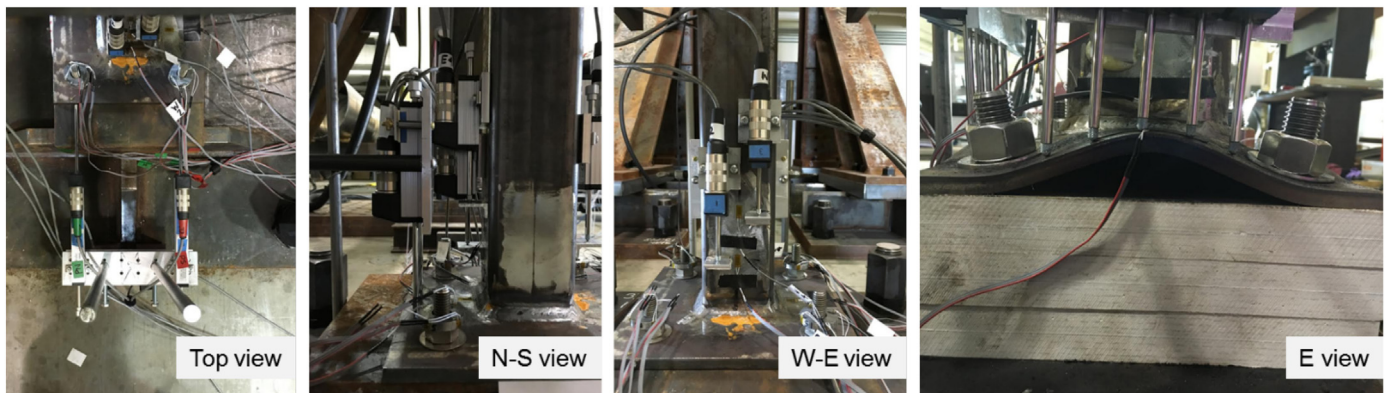


**Fig. 7.** Photographs of instrumentation plan from top, North to South, West to East, and East (east view is on a deformed specimen, demonstrating how LVDT sensors are able to read vertical deformations of base plate).

**Table 4**
Roof post results and nominal strength-to-predicted ratios.

| Test | STRENGTH RESULTS | | | | BASE PLATE YIELDING | | POST BENDING | |
|---|---|---|---|---|---|---|---|---|
| | $P_u$ | $R_f$ | $h$ | $M_u$ | $P_n$ | $P_u/P_n$ | $M_n$ | $M_u/M_n$ |
| Name | kN | – | m | kN-m | kN | – | kN-m | – |
| R1 | 23.73 | 0.85 | 0.533 | 10.76 | 68.49 | 0.35 | 10.26 | 1.05 |
| R2 | 37.09 | 0.85 | 0.533 | 16.82 | 68.49 | 0.30 | 10.26 | 1.64 |
| R4 | 24.76 | 0.85 | 0.533 | 11.23 | 68.49 | 0.36 | 10.26 | 1.09 |
| R5 | 38.65 | 0.85 | 0.381 | 12.52 | 121.8 | 0.32 | 10.26 | 1.22 |
| R7 | 30.60 | 0.95 | 0.533 | 15.51 | 121.8 | 0.25 | 10.26 | 1.51 |
| R8 | 41.32 | 0.95 | 0.381 | 14.96 | 121.8 | 0.34 | 10.26 | 1.46 |
| R9 | 28.64 | 0.95 | 0.381 | 10.36 | 121.8 | 0.24 | 10.26 | 1.01 |
| R10 | 41.99 | 0.95 | 0.381 | 15.20 | 121.8 | 0.34 | 10.26 | 1.48 |
| R11 | 41.30 | 0.95 | 0.381 | 14.95 | 121.8 | 0.34 | 10.26 | 1.46 |
| R12 | 40.21 | 0.95 | 0.381 | 14.56 | 121.8 | 0.33 | 10.26 | 1.42 |
| R13 | 41.41 | 0.95 | 0.381 | 14.99 | 121.8 | 0.34 | 10.26 | 1.46 |
| R14 | 38.65 | 0.95 | 0.381 | 13.99 | 121.8 | 0.32 | 10.26 | 1.36 |

| Test | FASTENER TENSION | | | FASTENER SHEAR | | FASTENER BENDING | | |
|---|---|---|---|---|---|---|---|---|
| | $T_{bn}$ | $T_{uplift}$ | $T_{uplift}/T_{bn}$ | $T_n$ | $P_u/T_n$ | $M_{bn}$ | $M_{bu}$ | $M_{bu}/M_{bn}$ |
| Name | kN | kN | – | kN | – | kN-m | kN-m | – |
| R1 | 136.2 | 70.58 | 0.52 | 164.2 | 0.14 | 0.22 | – | – |
| R2 | 136.2 | 110.3 | 0.81 | 164.2 | 0.23 | 0.22 | 2.83 | 13.07 |
| R3 | 136.2 | 68.34 | 0.50 | 164.2 | 0.12 | 0.22 | – | – |
| R4 | 136.2 | 73.67 | 0.54 | 164.2 | 0.15 | 0.22 | – | – |
| R5 | 136.2 | 82.14 | 0.60 | 164.2 | 0.24 | 0.22 | 2.95 | 13.62 |
| R7 | 176.9 | 101.8 | 0.58 | 212.2 | 0.14 | 0.42 | – | – |
| R8 | 176.9 | 98.20 | 0.56 | 212.2 | 0.19 | 0.42 | 3.15 | 7.48 |
| R9 | 176.9 | 68.01 | 0.38 | 212.2 | 0.13 | 0.42 | 2.18 | 5.18 |
| R10 | 176.9 | 99.72 | 0.56 | 212.2 | 0.20 | 0.42 | 3.20 | 7.60 |
| R11 | 176.9 | 98.09 | 0.55 | 212.2 | 0.19 | 0.42 | 3.15 | 7.47 |
| R12 | 176.9 | 95.51 | 0.54 | 212.2 | 0.19 | 0.42 | 3.06 | 7.28 |
| R13 | 176.9 | 98.35 | 0.56 | 212.2 | 0.20 | 0.42 | 1.05 | 2.50 |
| R14 | 176.9 | 91.80 | 0.52 | 212.2 | 0.18 | 0.42 | 5.89 | 14.0 |

transfer block, and includes the 25.4 mm top plate) to account for test rig influence on inflection point. These reduction factors, along with equations for all limit states, are explained in detail in [14]. Moment $M_u$ is calculated by multiplying $P_u$ by specimen height $h$ and the inflection point reduction factor $R_f$. Results are presented for the system, i.e., four fasteners are considered for shear and bending calculations. In the case of fastener tension ($T_{bn}$), two fastener are considered under uplift only ($T_{uplift,}$ caused by bending of the post). Nominal and measured results calculations are not available for all limit states (shim compression, for example, for which manufacturers do not typically provide nominal through-thickness compressive strengths).

Base plate yielding is characterized by yield line diagrams (developed and formalized via AISC Design Guide 6 [10]), and relationships for the yield load on the plate are determined from the diagram geometry, shown in Fig. 8.

The equations developed for these yield forces are provided in Eqs. 1 and 2 for the HSS 76x76x4.8 and HSS 102x102x12.7, respectively.

$$P = \frac{73F_y t^2}{24} \tag{1}$$

$$P = \frac{11F_y t^2}{4} \tag{2}$$

Shim compression for roof posts is determined via a combination of the applied axial force (44.5 kN or 10 kips) and the compression due to bending moment at the base plate at the maximum force. For canopy beams, which do not have applied axial load, shim compression is based solely on the compressive stresses from bending of the beam.

Based on the tabulated test-to-predicted ratios, fastener bending governs, and is magnified as shims increase in thickness. However, it should be noted that the required strengths for roof posts are approximately 6.8 kN-m (60 kip-inches, unfactored, and based upon common prototype design loads), during which the specimen responses are still
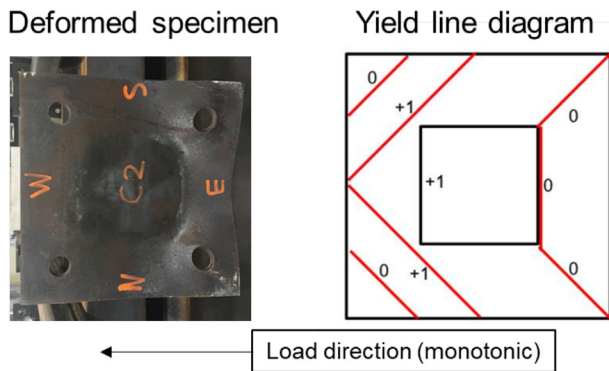
**Table 5**
Roof post results and measured test-to-predicted ratios.

| Test Name | STRENGTH RESULTS | | | | BASE PLATE YIELDING | | SHIM COMPRESSION | | | | |
|---|---|---|---|---|---|---|---|---|---|---|---|
| | $P_u$ | $R_f$ | $h$ | $M_u$ | $P_n$ | $P_u/P_n$ | $P_n$ | $P_{uB}$ | $P_{uA}$ | $P_{BA}$* | $P_{BA}/P_n$ |
| | kN | – | m | kN-m | kN | – | kN | kN | kN | kN | – |
| R1 | 23.73 | 0.85 | 0.533 | 10.76 | 78.20 | 0.30 | – | 70.58 | 44.48 | 115.1 | – |
| R2 | 37.09 | 0.85 | 0.533 | 16.82 | 208.7 | 0.18 | 10,296 | 110.3 | 44.48 | 154.8 | 0.02 |
| R4 | 24.76 | 0.85 | 0.533 | 11.23 | 78.20 | 0.32 | – | 73.67 | 44.48 | 118.1 | – |
| R5 | 38.65 | 0.85 | 0.381 | 12.52 | 208.7 | 0.19 | 10,296 | 82.14 | 44.48 | 126.6 | 0.01 |
| R7 | 30.60 | 0.95 | 0.533 | 15.51 | 208.7 | 0.15 | – | 101.8 | 44.48 | 146.2 | – |
| R8 | 41.32 | 0.95 | 0.381 | 14.96 | 208.7 | 0.20 | 10,296 | 98.20 | 44.48 | 142.7 | 0.01 |
| R9 | 28.64 | 0.95 | 0.381 | 10.36 | 208.7 | 0.14 | 5731.5 | 68.01 | 44.48 | 112.5 | 0.02 |
| R10 | 41.99 | 0.95 | 0.381 | 15.20 | 208.7 | 0.20 | 20,678 | 99.72 | 44.48 | 144.2 | 0.01 |
| R11 | 41.30 | 0.95 | 0.381 | 14.95 | 208.7 | 0.20 | 13,672 | 98.09 | 44.48 | 142.6 | 0.01 |
| R12 | 40.21 | 0.95 | 0.381 | 14.56 | 208.7 | 0.19 | 13,558 | 95.51 | 44.48 | 140.0 | 0.01 |
| R13 | 41.41 | 0.95 | 0.381 | 14.99 | 208.7 | 0.20 | 10,296 | 98.35 | 44.48 | 142.8 | 0.01 |
| R14 | 38.65 | 0.95 | 0.381 | 13.99 | 208.7 | 0.19 | 10,296 | 91.80 | 44.48 | 136.3 | 0.01 |

*$P_{BA} = P_{uB} + P_{uA}$

| Test Name | FASTENER TENSION | | | FASTENER SHEAR | | | | | | | |
|---|---|---|---|---|---|---|---|---|---|---|---|
| | $T_{bn}$ | $T_{uplift}$ | $T_{uplift}/T_{bn}$ | $T_n$ | $P_u/T_n$ | | | | | | |
| | kN | kN | – | kN | – | | | | | | |
| R1 | 177.6 | 70.58 | 0.40 | 213.1 | 0.11 | | | | | | |
| R2 | 177.6 | 110.3 | 0.62 | 213.1 | 0.17 | | | | | | |
| R3 | 177.6 | 68.34 | 0.38 | 213.1 | 0.09 | | | | | | |
| R4 | 177.6 | 73.67 | 0.41 | 213.1 | 0.12 | | | | | | |
| R5 | 177.6 | 82.14 | 0.46 | 213.1 | 0.18 | | | | | | |
| R7 | 283.9 | 101.8 | 0.36 | 340.7 | 0.09 | | | | | | |
| R8 | 283.9 | 98.20 | 0.35 | 340.7 | 0.12 | | | | | | |
| R9 | 283.9 | 68.01 | 0.24 | 340.7 | 0.08 | | | | | | |
| R10 | 283.9 | 99.72 | 0.35 | 340.7 | 0.12 | | | | | | |
| R11 | 283.9 | 98.09 | 0.35 | 340.7 | 0.12 | | | | | | |
| R12 | 283.9 | 95.51 | 0.34 | 340.7 | 0.12 | | | | | | |
| R13 | 283.9 | 98.35 | 0.35 | 340.7 | 0.12 | | | | | | |
| R14 | 283.9 | 91.80 | 0.32 | 340.7 | 0.11 | | | | | | |

## Deformed specimen

## Yield line diagram



Load direction (monotonic)

**Fig. 8.** Yield line diagram for base plates and post/beams, based on observed deformed shapes.

**Table 6**
Canopy beam results and nominal strength-to-predicted ratios.

| | STRENGTH RESULTS | | | | BASE PLATE YIELDING | | POST BENDING | |
|---|---|---|---|---|---|---|---|---|
| Test | $P_u$ | $R_f$ | h | $M_u$ | $P_n$ | $P_u/P_n$ | $M_n$ | $M_u/M_n$ |
| Name | kN | – | m | kN-m | kN | – | kN-m | – |
| C1 | 21.74 | 0.80 | 1.448 | 25.18 | 61.92 | 0.35 | 40.06 | 0.63 |
| C2 | 25.83 | 0.80 | 1.295 | 26.77 | 61.92 | 0.42 | 40.06 | 0.67 |
| C4 | 20.19 | 0.80 | 1.448 | 23.38 | 61.92 | 0.33 | 40.06 | 0.58 |
| C5 | 21.61 | 0.80 | 1.295 | 22.39 | 61.92 | 0.35 | 40.06 | 0.56 |
| C7 | 27.64 | 0.95 | 1.448 | 38.01 | 110.1 | 0.25 | 40.06 | 0.95 |
| C8 | 31.31 | 0.95 | 1.295 | 38.54 | 110.1 | 0.28 | 40.06 | 0.96 |
| C9 | 30.03 | 0.95 | 1.295 | 36.96 | 110.1 | 0.27 | 40.06 | 0.92 |
| C10 | 32.19 | 0.95 | 1.295 | 39.61 | 110.1 | 0.29 | 40.06 | 0.99 |
| C11 | 30.97 | 0.95 | 1.295 | 38.11 | 110.1 | 0.28 | 40.06 | 0.95 |
| C12 | 31.92 | 0.95 | 1.295 | 39.28 | 110.1 | 0.29 | 40.06 | 0.98 |
| C13 | 31.28 | 0.95 | 1.295 | 38.49 | 110.1 | 0.28 | 40.06 | 0.96 |
| C15 | 30.26 | 0.95 | 1.295 | 37.24 | 110.1 | 0.27 | 40.06 | 0.93 |

| | FASTENER TENSION | | | FASTENER SHEAR | | FASTENER BENDING | | |
|---|---|---|---|---|---|---|---|---|
| Test | $T_{bn}$ | $T_{uplift}$ | $T_{uplift}/T_{bn}$ | $T_n$ | $P_u/T_n$ | $M_{bn}$ | $M_{bu}$ | $M_{bu}/M_{bn}$ |
| Name | kN | kN | – | kN | – | kN-m | kN-m | – |
| C1 | 306.6 | 165.2 | 0.54 | 369.4 | 0.06 | 0.73 | | |
| C2 | 306.6 | 175.6 | 0.57 | 369.4 | 0.07 | 0.73 | 1.97 | 2.70 |
| C4 | 306.6 | 153.4 | 0.50 | 369.4 | 0.05 | 0.73 | – | – |
| C5 | 306.6 | 146.9 | 0.48 | 369.4 | 0.06 | 0.73 | 1.65 | 2.26 |
| C7 | 314.4 | 249.4 | 0.79 | 377.3 | 0.07 | 1.00 | – | – |
| C8 | 314.4 | 252.9 | 0.80 | 377.3 | 0.08 | 1.00 | 2.39 | 2.39 |
| C9 | 314.4 | 242.5 | 0.77 | 377.3 | 0.08 | 1.00 | 2.29 | 2.29 |
| C10 | 314.4 | 259.9 | 0.83 | 377.3 | 0.09 | 1.00 | 2.45 | 2.46 |
| C11 | 314.4 | 250.1 | 0.80 | 377.3 | 0.08 | 1.00 | 2.36 | 2.36 |
| C12 | 314.4 | 257.7 | 0.82 | 377.3 | 0.08 | 1.00 | 2.43 | 2.44 |
| C13 | 314.4 | 252.6 | 0.80 | 377.3 | 0.08 | 1.00 | 0.79 | 0.80 |
| C15 | 314.4 | 244.4 | 0.78 | 377.3 | 0.08 | 1.00 | 4.61 | 4.62 |

elastic, so all specimens resisted loads well in excess of typical factored design loads.

Roof posts were observed to bend significantly at the base plate, regardless of plate slenderness. The deformation of the plate allowed the post to rotate about the base plate. As such, stresses were concentrated on the CJP weld, and failure in all specimens ultimately occurred in the heat-affected zone of the weld. In typical roof post details, the base plate is selected based upon economy and rules of thumb and is often significantly over-designed for the detail. Thus, the weld between the post and the base plate may be the limiting factor in a typical design, as it was in the specimen design. However, the weld limit states did not engage in the specimen behavior until beyond 10% drift.

Shims were lightly exercised by the loading, as evidenced by the test-to-predicted ratios. As shims should match the base plate area for maximum thermal performance, shims are large, and forces evenly distributed across the shim. Shims were not observed to rack back and forth during testing, except in the final stages of lateral loading, when fastener bearing on the shims caused the shims to rub against one another.

Results and nominal test-to-predicted ratios for the canopy beams are presented in Table 6 below. Limit states and strength results are determined in the same manner as in the roof post result tables. Results with measured properties are presented in Table 7.

Canopy beams, despite representing an entirely different structural detail from the roof posts, behave similarly. Fastener bending governs but increased fastener sizes mitigate this limit state more so than in the roof post testing. Canopy beam base plates also deformed significantly during testing, and the yield line methodology is again considered an over-estimate of the strength of these base plates.

Fig. 9 depicts moment-drift results using the force from the horizontal actuator, as well as backbone curves from the cyclic testing. Notably, the shim material does not have a significant impact on peak moment. Roof posts are more variable in response than canopy beams, but in both sub-assemblies, nominally identical specimens (save for shim material and thickness) varied by no more than 15%. As shims were not loaded near their maximum capacity, this is anticipated for canopy beams. Roof post testing exercised the shims with an additional 44.5 kN (10 kips) of axial load, so variability in the force results up to 5% drift may be attributed to compression of the shims (though not failure). Performance is striated based upon shim compressive strength. Polyurethane shims are consistently the strongest shim material and phenolic consistently the weakest. Across testing, fastener size and base plate thickness dictate behavior more than fastener material, shim material, and shim thickness.

Representative cyclic plots are shown in Fig. 10 below for tests C7 and C10, demonstrating the range in behavior between an unmitigated specimen and a specimen with 76.2 mm (3 in.) shims. As anticipated, due to the shorter beam height, the shimmed specimen reaches higher moments. Both specimens demonstrate slight pinching, and this behavior is visible in all of the roof posts and canopy beams tested. Pinching in the reverse cycle can be attributed to a stability plate buckling mode as the base plate moves from buckling from loaded edge to loaded edge. Fastener elongation and base plate deformation contribute to damage in the specimen, which reduces its energy dissipating capacity. Generally, data for all tests are provided in [14] in their entirety.

Base plate strains (as measured by a strain gauge installed on the east side of the base plate) are shown for unmitigated posts and beams and posts and beams mitigated with vinylester shims (shown in Fig. 11 and Fig. 12 respectively). For canopy beams, the elongated specimen size increases strains on the base plate in specimens with thicker plates (C7–15). Shims of increasing thickness contribute to larger strains in the base plate for canopy beams only, in part due to the longer length of the total specimen with the addition of thick shims.

In the roof posts tests, where axial load is applied prior to lateral loading, posts with thinner base plates experience greater base plate strains than those specimens with thicker plates. Shim thickness has no discernible effect on the base plate strains.

Base plate vertical LVDTs (quintuplet sensors) installed on the south and east faces of the base plate capture base plate deformed shapes as the test progresses. While the sensors were removed just beyond 2% drift to prevent damage to the sensors, they recorded behavior in the design region for these cladding details. Fig. 13 presents representative plots of these deformed shapes for tests R7 and R10, which are nominally identical except for the 76.2 mm (3 in.) shim in R10. The plotted deformed shape is with respect to the base plate and does not capture global movement of the base plate (and therefore any shim compression). While R10 does experience larger deformations on the east base plate, the two deformed shapes are within 10% of each other.

Fastener strains as measured with the load cell on the south side are shown for roof posts and canopy beams in Fig. 14 and Fig. 15 respectively. Fastener load cell strain gauges (four per gauge) are averaged

**Table 7**
Canopy beam results and measured test-to-predicted ratios.

| Test Name | STRENGTH RESULTS | | | | BASE PLATE YIELDING | | SHIM COMPRESSION | | | | |
|---|---|---|---|---|---|---|---|---|---|---|---|
| | $P_u$ | $R_f$ | $h$ | $M_u$ | $P_n$ | $P_u/P_n$ | $P_n$ | $P_{uB}$ | $P_{uA}$ | $P_{BA}$* | $P_{BA}/P_n$ |
| | kN | – | m | kN-m | kN | – | kN | kN | kN | kN | – |
| C1 | 21.74 | 0.80 | 1.448 | 25.18 | 70.70 | 0.31 | 0 | 165.20 | 0 | 165.20 | – |
| C2 | 25.83 | 0.80 | 1.295 | 26.77 | 70.70 | 0.37 | 10,296 | 175.64 | 0 | 175.64 | 0.02 |
| C4 | 20.19 | 0.80 | 1.448 | 23.38 | 70.70 | 0.29 | 0 | 153.44 | 0 | 153.44 | – |
| C5 | 21.61 | 0.80 | 1.295 | 22.39 | 70.70 | 0.31 | 10,296 | 146.94 | 0 | 146.94 | 0.01 |
| C7 | 27.64 | 0.95 | 1.448 | 38.01 | 188.7 | 0.15 | 0 | 249.41 | 0 | 249.41 | – |
| C8 | 31.31 | 0.95 | 1.295 | 38.54 | 188.7 | 0.17 | 10,296 | 252.86 | 0 | 252.86 | 0.02 |
| C9 | 30.03 | 0.95 | 1.295 | 36.96 | 188.7 | 0.16 | 5731 | 242.52 | 0 | 242.52 | 0.04 |
| C10 | 32.19 | 0.95 | 1.295 | 39.61 | 188.7 | 0.17 | 20,678 | 259.90 | 0 | 259.90 | 0.01 |
| C11 | 30.97 | 0.95 | 1.295 | 38.11 | 188.7 | 0.16 | 13,672 | 250.06 | 0 | 250.06 | 0.02 |
| C12 | 31.92 | 0.95 | 1.295 | 39.28 | 188.7 | 0.17 | 13,558 | 257.74 | 0 | 257.74 | 0.02 |
| C13 | 31.28 | 0.95 | 1.295 | 38.49 | 188.7 | 0.17 | 10,296 | 252.57 | 0 | 252.57 | 0.02 |
| C15 | 30.26 | 0.95 | 1.295 | 37.24 | 188.7 | 0.16 | 10,296 | 244.38 | 0 | 244.38 | 0.02 |

*$P_{BA} = P_{uB} + P_{uA}$

| Test Name | FASTENER TENSION | | | FASTNER SHEAR | |
|---|---|---|---|---|---|
| | $T_{bn}$ | $T_{uplift}$ | $T_{uplift}/T_{bn}$ | $T_n$ | $P_u/T_n$ |
| | kN | kN | – | kN | – |
| C1 | 399.5 | 165.2 | 0.41 | 479.4 | 0.05 |
| C2 | 399.5 | 175.6 | 0.44 | 479.4 | 0.05 |
| C4 | 399.5 | 153.4 | 0.38 | 479.4 | 0.04 |
| C5 | 399.5 | 146.9 | 0.37 | 479.4 | 0.05 |
| C7 | 504.7 | 249.4 | 0.49 | 605.7 | 0.05 |
| C8 | 504.7 | 252.9 | 0.50 | 605.7 | 0.05 |
| C9 | 504.7 | 242.5 | 0.48 | 605.7 | 0.05 |
| C10 | 504.7 | 259.9 | 0.51 | 605.7 | 0.05 |
| C11 | 504.7 | 250.1 | 0.50 | 605.7 | 0.05 |
| C12 | 504.7 | 257.7 | 0.51 | 605.7 | 0.05 |
| C13 | 504.7 | 252.6 | 0.50 | 605.7 | 0.05 |
| C15 | 504.7 | 244.4 | 0.48 | 605.7 | 0.05 |
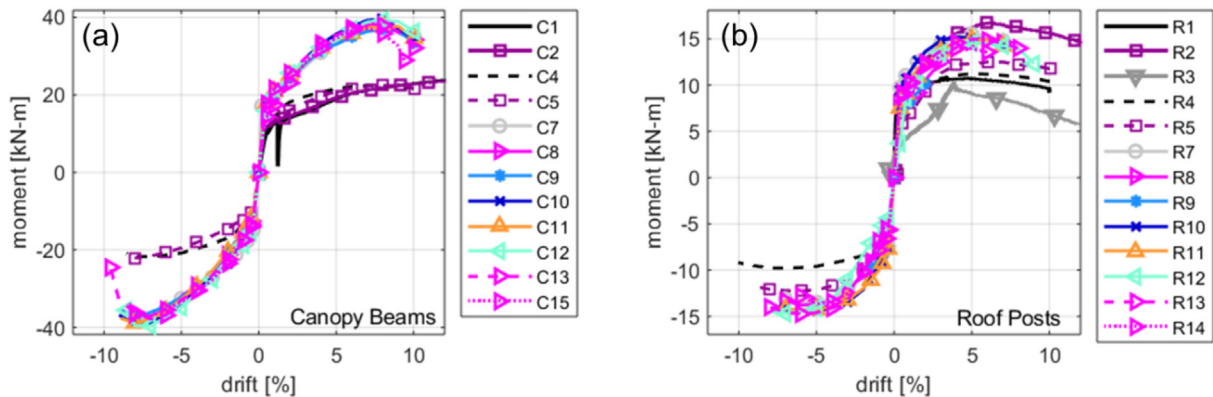


**Fig. 9.** Cyclic backbone and monotonic force-drift results for (a) canopy beam and (b) roof post specimens.
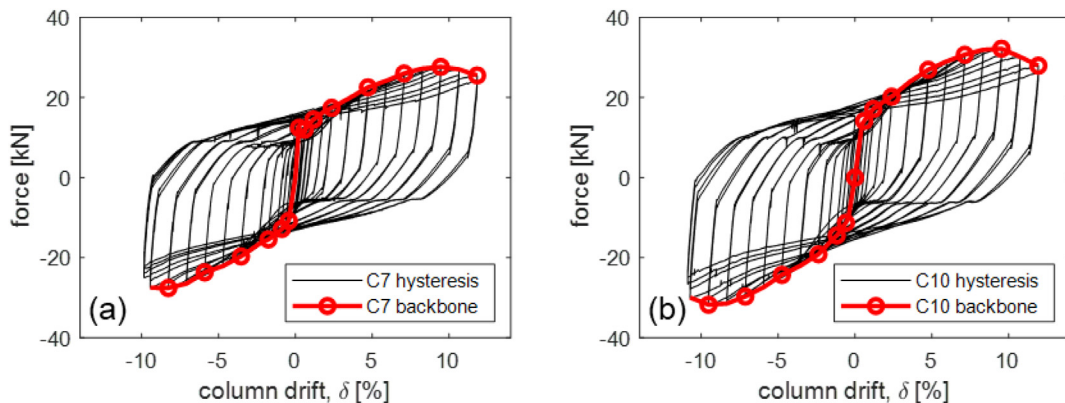


**Fig. 10.** Hysteretic curves and backbones for tests (a) C7 (no shim) and (b) C10 (76.2 mm (3 in.) polyurethane shim).
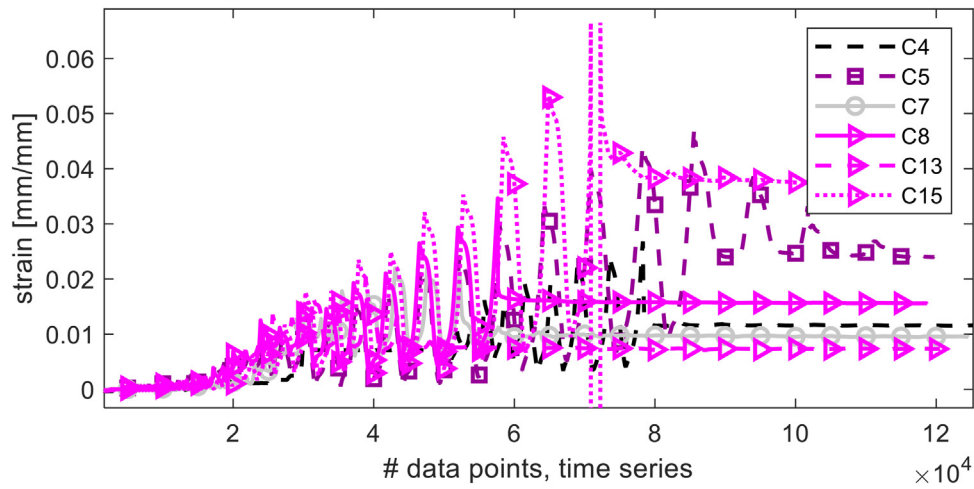
**Fig. 11.** East side (loaded side) base plate strains for unmitigated canopy beams and assemblies with vinylester shims of varying thickness.
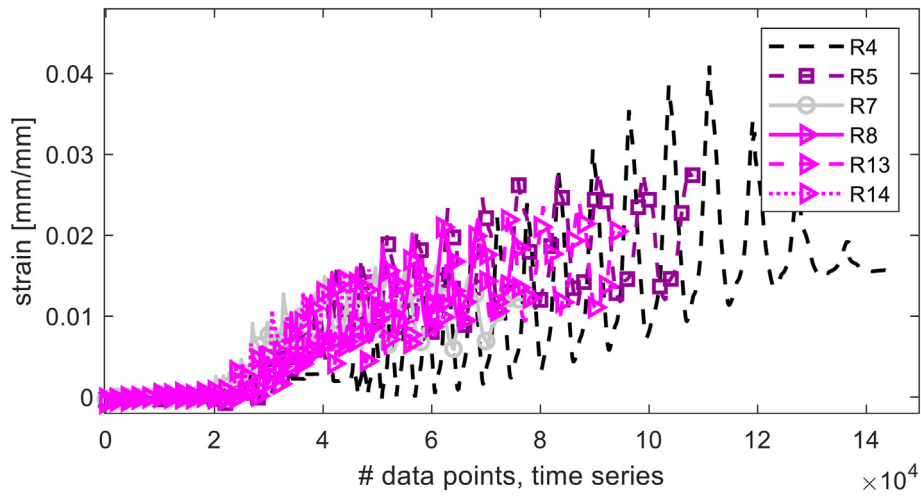


**Fig. 12.** East side (loaded side) base plate strains for unmitigated roof posts and assemblies with vinylester shims of varying thickness.
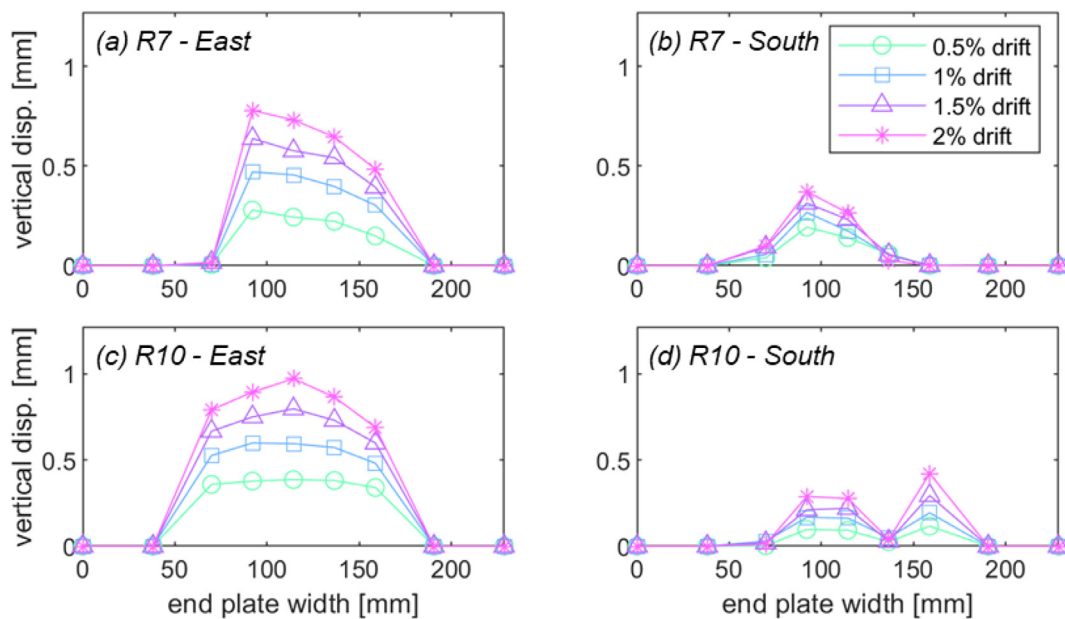


**Fig. 13.** Base plate vertical LVDT sensors at design drift levels for (a) R7 with no shims (b) R7 with 76.2 mm (3 in.) vinylester shims (c) R10 with no shims (d) R10 with 76.2 mm vinylester shims on the south and east faces of the base plate. Specimens are otherwise nominally identical.
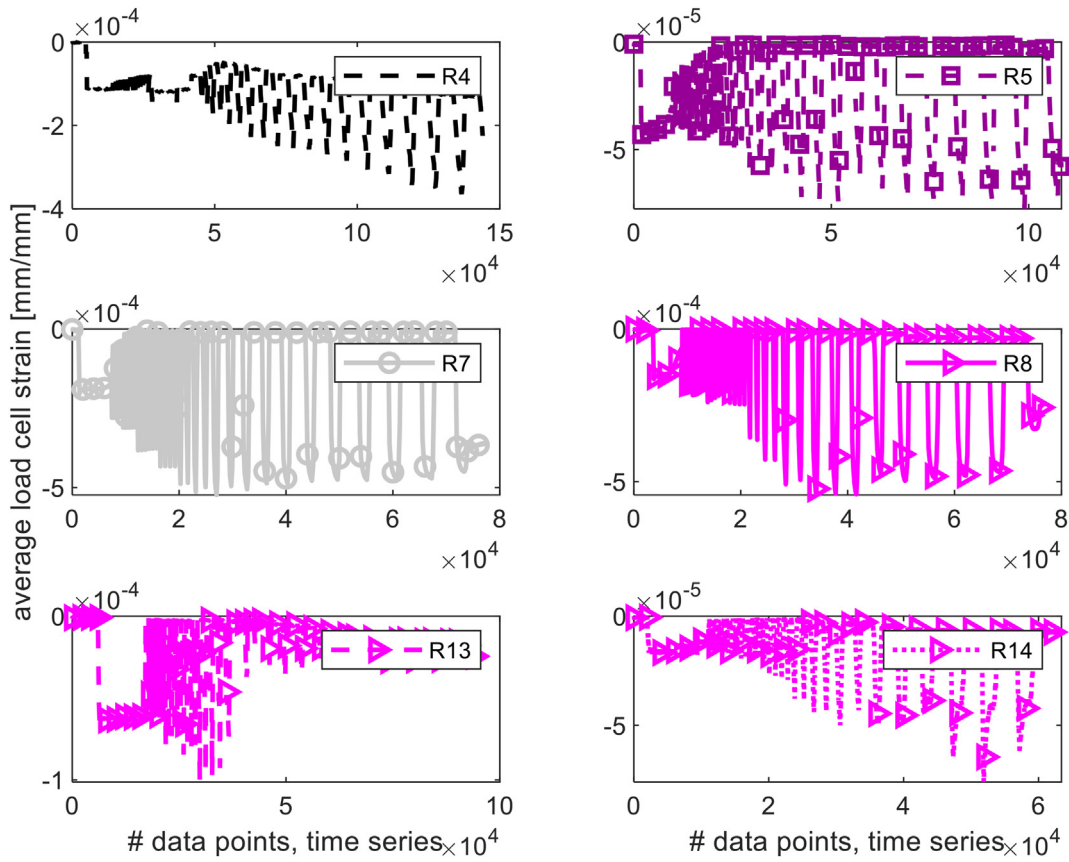
**Fig. 14.** Average fastener load cell strain in South load cells for unmitigated roof posts and roof posts with vinylester shims.
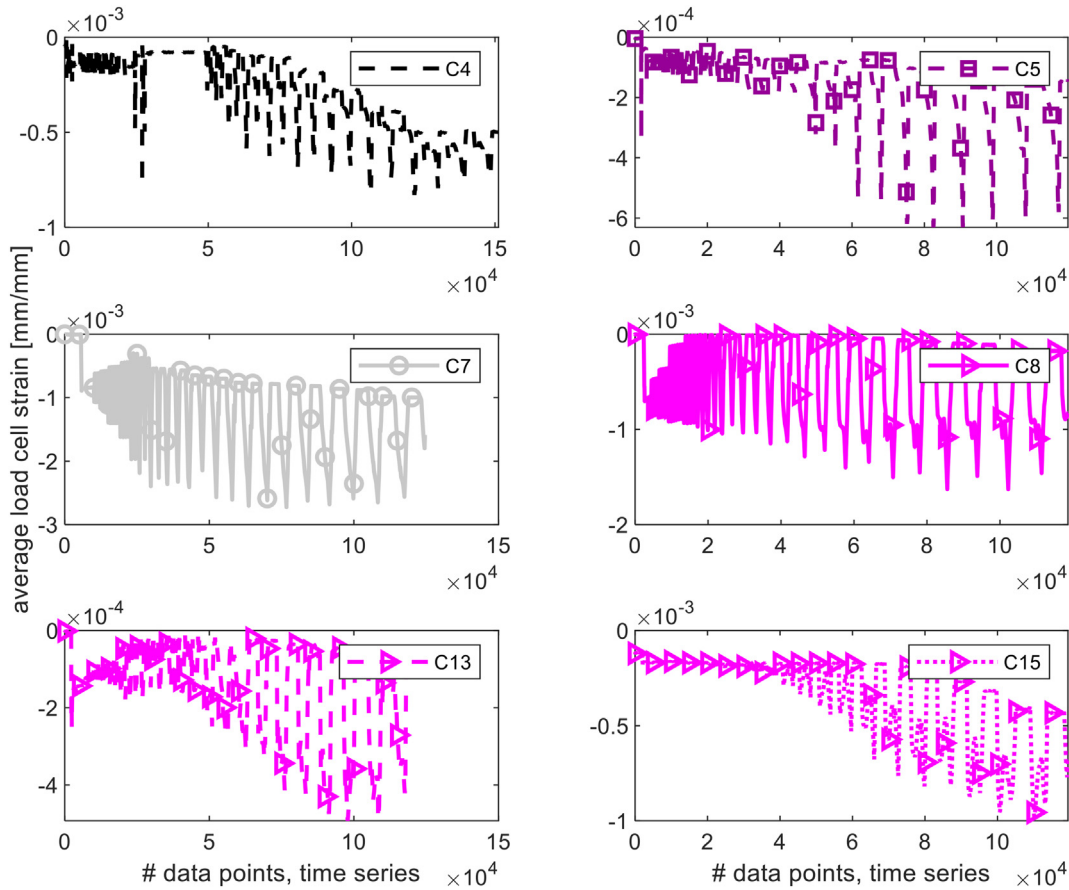


**Fig. 15.** Average fastener load cell strain in South load cells for unmitigated canopy beams and canopy beams with vinylester shims.
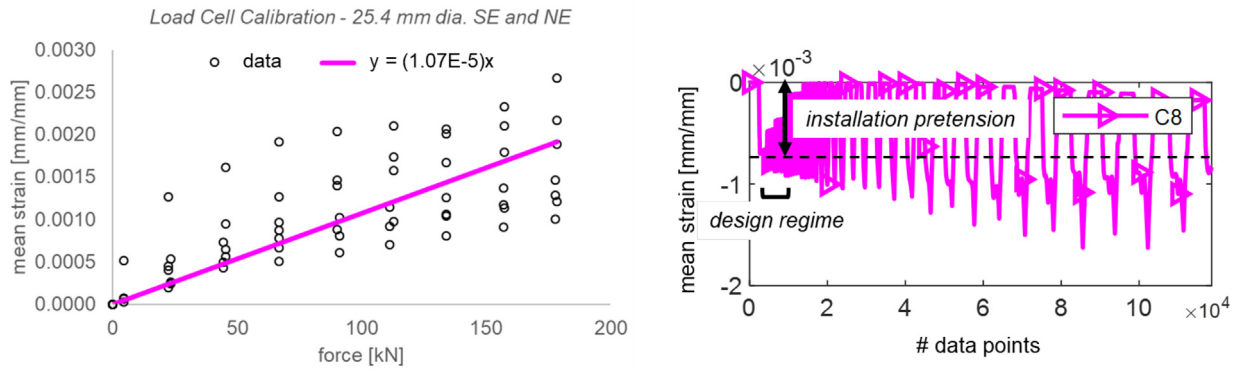
**Fig. 16.** At left, load cell calibration curve, with curve fit, at right, detail of Fig. 14 demonstrating design regime and installation pretension on fastener.

to produce one measurement per load cell (per fastener). Load cells were pre-tensioned while data was recorded, and then zeroed immediately before application of load. Examining the progression of peaks in load cell strain from cyclic data, it is clear that these peaks plateau, despite the progressing load protocol. Thus, after initial loading cycles, tension in the fasteners remains approximately constant throughout the test.

Strains from the load cells may be converted to axial force in the fasteners via the load cell calibration curves for each load cell, shown for two of the 25.4 mm (1 in.) diameter load cells in the figure below. This calibration was performed in an MTS universal testing machine prior to testing. Load cells were compressed and readings from the load cell strain gauges were recorded at ten force levels. Applied

compression did not exceed or approach the yield stress of the load cells. A linear curve fit is performed on the data, yielding the relationship between stress and applied force as shown in the figure, where the variable y is defined as strain and x is defined as force (see Fig. 16). Rearranging terms, anchor force = 93,500 * strain. Using this relationship, it is possible to estimate the force in the load cells and also the compression in the shims at the fastener location.

Fig. 16 examines test C8. In the design regime (up to 9.5 kN-m of moment) average load cell strain consistently remains below 0.001 mm/mm. Using this value and the load cell calibration curves, the force in the fastener is estimated to be 89 kN (20 kips). Assuming that this anchor force is transmitted to the shims via the washers, which, for 25.4 mm (1 in.) fasteners have an area of 1452 mm² (2.25 in²), the stress
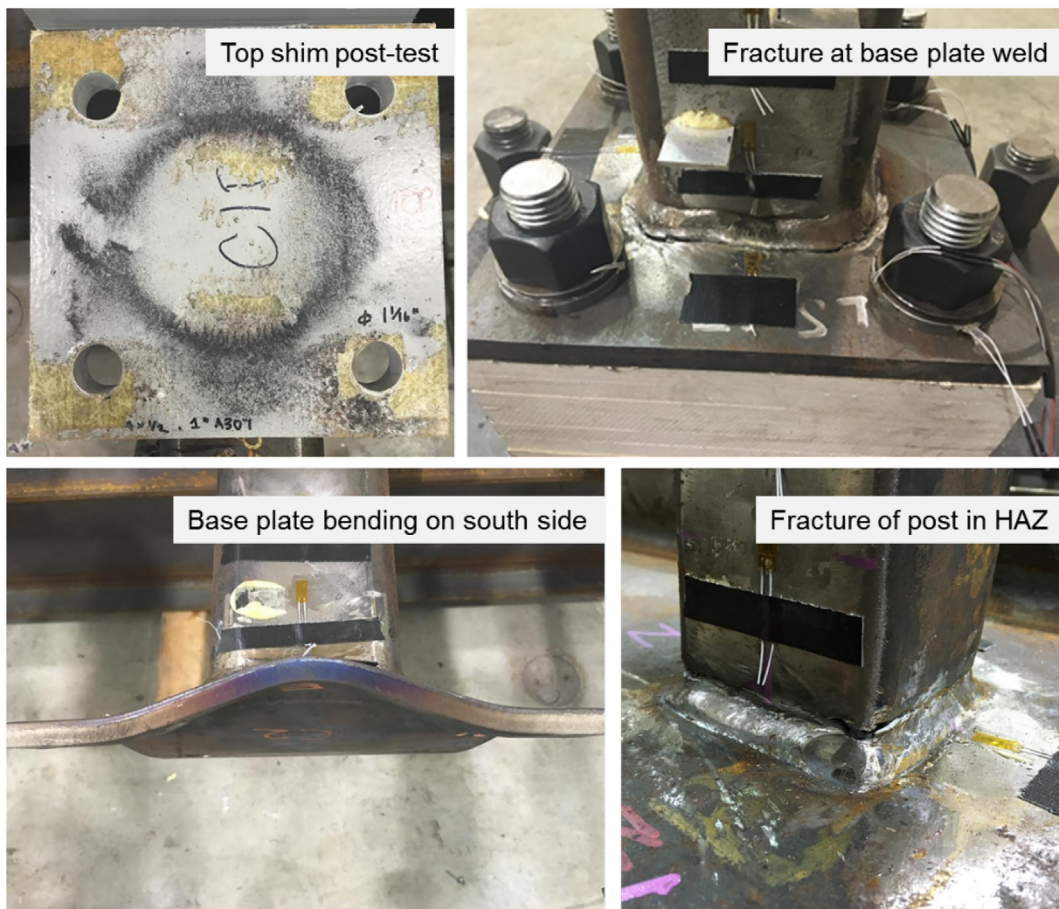


**Fig. 17.** Photographs of typical failure modes for roof posts and canopy beams.

in the shims under the washers is 89 kN/1452 mm$^2$ = 61 MPa (20 kips/ 2.25 in$^2$ = 8.89 ksi). This calculation assumes all stress is concentrated in the washer area and is not distributed to the remainder of the shim. For vinylester shims, as in test C8, 61 MPa (8.89 ksi) represents less than 30% of ultimate stress (205 MPa, from Table 1). It is noted that strains from the roof post testing were significantly lower than those recorded in the canopy beam testing and the example presented here represents a conservative scenario.

Photographs of typical failure modes are shown in Fig. 17 below. The shims remained unaffected by the loading, save for rubbing of the paint finish from the surface of the shim. Holes were not ovalized, and there were no delaminations or failures at the bond line. Fracture of the specimen occurred either in the post/beam above the weld, or in the base plate, below the weld. Fractures universally occurred within the heat-effected zone of the weld (HAZ). Base plate bending was pervasive and began at the initiation of lateral load. While base plate deformations were significant across all base plate thicknesses, they were magnified for thinner base plates (pictured).

## 4. Conclusions and design recommendations

Fiber reinforced polymer shims are a viable option for thermal breaks in discrete steel structural elements which span the building envelope. The research program described herein involved experimental testing of canopy beam and roof post archetypes with five different shim materials acting as thermal breaks. The thicknesses of these shims were varied to match possible insulation layers and provide maximum effectiveness as thermal breaks. Experimental results indicate that specimens with FRP shims perform adequately under service loads, considering both monotonic and cyclic loading. Shims in particular experience low compressive stresses and as a result do not contribute to overall specimen response. After testing, these shims were observed to be undamaged. Shim material properties, while varied across specimens, did not impact flexural capacity for the canopy beams, and had a modest impact on roof post flexural capacity, as indicated by variations at peak experimental loads corresponding to shim material. Fastener elongation and bending and base plate yielding governed deformation response. Canopy beams and roof posts with shims between the base plate and the support structure may be designed using typical North American industry practices modified to account for the shims, assuming the shims match the base plate size. Specifically:

- Determine the compression stress in the shims and the tensile force in the fasteners using elastic analysis, assuming plane sections remain planar. For roof posts with axial load, an iterative solution is required to find the neutral axis. This approach may also be used to estimate the contribution of the shims to bending deflection.

- Neglect the shims when designing for shear below the base plate. Rely on single-curvature fastener bending to resist shear forces. Combine the fastener tensile and bending effects in accordance with AISC combined force equations. This approach may also be used to estimate the contribution of the shims to shear deflection.

The authors caution against using shims in moderately- or heavily-loaded connections without further research. The work herein examined only lightly-loaded structural archetypes where the shims are not significantly compressed. Creep should be considered, and is discussed extensively in [14]. Any perceived benefit to the system strength stemming from the inclusion of shims is attributed to the shortened beam-column height. Rather, shims should be considered as "not-detrimental" to the system performance rather than beneficial. If shims increase total beam-column height, the change in moment-to-shear ratio should be assessed by the designer.

## Declaration of Competing Interest

The authors declare that they have no known competing financial interests or personal relationships that could have appeared to influence the work reported in this paper.

## References

[1] AISC (American Institute of Steel Construction), Specification for structural steel buildings, ANSI / AISC 360-16, American Institute of Steel Construction (2016) 1–676.
[2] AISC (American Institute of Steel Construction), Seismic provisions for structural steel buildings, ANSI / AISC 341-16, American Institute of Steel Construction (2016) 1–480.
[3] American Society for Heating, Refrigeration, and Air-Conditioning Engineers, ANSI/ASHRAE/IES Standard 90.1–2019 – Energy Standard for Buildings Except Low-Rise Residential Buildings, American Society for Heating, Refrigeration, and Air-Conditioning Engineers (ASHRAE), 2019.
[4] American Society for Heating, Refrigeration, and Air-Conditioning Engineers, ASHRAE 1365-RP Thermal Performance of Building Envelope Details for Mid- and High-Rise Buildings, American Society of Heating, Refrigeration, and Air-Conditioning Engineers (ASHRAE), 2011.
[5] ASTM International, A193/A193M — 20: Standard Specification for Alloy-Steel and Stainless Steel Bolting for High Temperature or High Pressure Service and Other Special Purpose Applications, ASTM International, West Conshohoken, PA, USA, 2020.
[6] ASTM International, A307/A307M - 14e1: Standard Specification for Carbon Steel Bolts, Studs, and Threaded Rod 60000 PSI Tensile Strength, ASTM International, West Conshohoken, PA, USA, 2014.
[7] Corus Group plc, Avoidance of Thermal Bridging in Steel Construction, The Steel Construction Institute, Ascot, United Kingdom, 2008.
[8] J.M. Fisher, L.A. Kloiber, "AISC Design Guide 1: Base Plate and Anchor Rod Design." Chicago, 2006.
[9] I. Gomez, A. Kanvinde, C. Smith, G. Deierlein, "Shear Transfer in Exposed Column Base Plates." Chicago, https://www.aisc.org/uploadedFiles/Research/Research_Reports/Kanvinde-ShearTransferinExposedColumnBasePlates.pdf 2009.
[10] T.M. Murray, W.L. Shoemaker, AISC Design Guide 16: Flush and Extended Multiple-Row Moment End-Plate Connections, American Institute of Steel Construction, Chicago, 2002.
[11] Morrison Hershfield, Thermal Performance of Building Envelope Details for Mid- and High-Rise Builds, Morrison Hershfield, New York, New York, 2011.
[14] K.D. Peterman, J. Kordas, J. Moradei, K. Coleman, J.F. Hajjar, J.A. Aloisio, M.D. Webster, Thermal Break Strategies for Cladding Systems in Building Structures, 2017.
[15] S.P. White, S. Hamel, "Thermo-Mechanical Modeling of Thermal Breaks in Structural Steel Point Transmittances." Chicago, https://www.aisc.org/globalassets/aisc/research-library/thermal-breaks-in-structural-steel-point-transmittances-hamel.pdf 2016.